Oscillating collective motion of active rotors in confinement

Peng Liu[a,b,c,1], Hongwei Zhu[d,1], Ying Zeng[e,1], Guangle Du[a,b,c,f], Luhui Ning[a,b,c], Dunyou Wang[g], Ke Chen[a,b,c,h], Ying Lu[a,b,c,h], Ning Zheng[d,2], Fangfu Ye[a,b,c,f,h,2], and Mingcheng Yang[a,b,c,2]

[a]Beijing National Laboratory for Condensed Matter Physics, Institute of Physics, Chinese Academy of Sciences, Beijing 100190, China; [b]Laboratory of Soft Matter Physics, Institute of Physics, Chinese Academy of Sciences, Beijing 100190, China; [c]School of Physical Sciences, University of Chinese Academy of Sciences, Beijing 100049, China; [d]School of Physics, Beijing Institute of Technology, Beijing 100081, China [e]Research Center of Computational Physics, School of Mathematics and Physics, Mianyang Teachers' College, Mianyang 621000, China; [f]Wenzhou Institute, University of Chinese Academy of Sciences, Wenzhou, Zhejiang 325001, China; [g]College of Physics and Electronics, Shandong Normal University, Jinan 250014, China; and [h]Songshan Lake Materials Laboratory, Dongguan, Guangdong 523808, China

Edited by David A. Weitz, Harvard University, Cambridge, MA, and approved April 15, 2020 (received for review December 23, 2019)

Due to its inherent out-of-equilibrium nature, active matter in confinement may exhibit collective behavior absent in unconfined systems. Extensive studies have indicated that hydrodynamic or steric interactions between active particles and boundary play an important role in the emergence of collective behavior. However, besides introducing external couplings at the single-particle level, the confinement also induces an inhomogeneous density distribution due to particle-position correlations, whose effect on collective behavior remains unclear. Here, we investigate this effect in a minimal chiral active matter composed of self-spinning rotors through simulation, experiment, and theory. We find that the density inhomogeneity leads to a position-dependent frictional stress that results from interrotor friction and couples the spin to the translation of the particles, which can then drive a striking spatially oscillating collective motion of the chiral active matter along the confinement boundary. Moreover, depending on the oscillation properties, the collective behavior has three different modes as the packing fraction varies. The structural origins of the transitions between the different modes are well identified by the percolation of solid-like regions or the occurrence of defect-induced particle rearrangement. Our results thus show that the confinement-induced inhomogeneity, dynamic structure, and compressibility have significant influences on collective behavior of active matter and should be properly taken into account.

confinement | collective behavior | chiral active matter | rotor

Active matter has attracted considerable interest in the past two decades due to its intrinsic nonequilibrium nature and potential applications in microdevices and smart materials (1–6). In active-matter systems, the constituent particles individually convert stored or ambient energy into particle motility: self-propelled translation (7–9) or rotation (10–15). The active matter often exhibits exotic nonequilibrium phenomena, among which the emergent collective behavior of active particles is especially intriguing (16–22).

Thanks to the motility of active particles, the role played by originally trivial ingredients in passive systems becomes extremely subtle and important in active systems. A relevant example is that the confinement wall in an active system not only prevents the particles from escaping and introduces surface tension, as in equilibrium cases, but also gives rise to collective motion of active particles, which is otherwise absent. For instance, sperm cells and microorganisms form rotating clusters near the substrate (23–25), colloidal surfers on the substrate aggregate into living crystals (26), and colloidal rollers and bacteria confined by side walls self-organize into vortex patterns (27–29). In these situations, the hydrodynamic interactions between the boundary and the active particles are critical to the emergence of collective behavior.

In this article, we study how confinement may influence the nonequilibrium collective dynamics of interacting active rotors. Compared with their translational counterparts, systems composed of active rotors remain much less explored. Nevertheless, as a representative chiral active matter that breaks both parity and time-reversal symmetries, the active-rotor systems have recently been the subject of fundamental theoretical interest (30, 31). It has been reported that a fluid of interacting rotors in confinement yields a collective edge flow parallel to the boundary (12, 32, 33), which is proven to be even topologically protected (34). In this case, the steric particle–boundary interactions impose a boundary condition that allows the conversion of spin-angular momentum into "orbital" angular momentum. However, apart from the steric interactions with the particles, confinement can also cause a spatially nonuniform distribution of particle-number density (35, 36). The density inhomogeneity is ubiquitous in confined interacting many-body systems and could have unexpected effects on collective behavior. Here, we numerically and experimentally investigate the effects of the density inhomogeneity on the emergent collective behavior in a confined chiral active matter. We show that the density inhomogeneity can give rise to a spatially oscillating edge flow, and its underlying mechanism is clarified through a continuum hydrodynamic theory with a density-dependent antisymmetric

Significance

The exploration of chiral active matter composed of self-spinning objects, which breaks both parity and time-reversal symmetries, is an exciting and rapidly developing area. A particularly interesting phenomenon of chiral active matter is the emergence of a spontaneous unidirectional collective edge flow in confinement, with potentials for robust material transport. This unique feature has generally been discussed in the context of incompressible and structureless homogeneous fluid. Here, we show that confinement-induced nonuniform distribution of spinners greatly influences the edge flow, causing a spatially oscillatory pattern. Moreover, as the structure of the active media varies, different collective modes emerge. These findings significantly advance our understanding of collective behavior of chiral active matter in confinement.

Author contributions: N.Z., F.Y., and M.Y. designed research; P.L., H.Z., Y.Z., G.D., N.Z., F.Y., and M.Y. performed research; P.L., H.Z., Y.Z., G.D., L.N., D.W., K.C., Y.L., N.Z., F.Y., and M.Y. analyzed data; and P.L., N.Z., F.Y., and M.Y. wrote the paper.

The authors declare no competing interest.

This article is a PNAS Direct Submission.

[1]P.L., H.Z., and Y.Z. contributed equally to this work.

[2]To whom correspondence may be addressed. Email: fye@iphy.ac.cn, ningzheng@bit.edu.cn, or mcyang@iphy.ac.cn.

This article contains supporting information online at https://www.pnas.org/lookup/suppl/doi:10.1073/pnas.1922633117/-/DCSupplemental.

First published May 19, 2020.

frictional stress. Furthermore, we identify three different collective modes of motion and their respective structural origins.

Results

The simulation system consists of N spinning disks of diameter σ_s confined in a circular boundary of radius R, as shown in Fig. 1*A*. Each constituent disk spins counterclockwise, driven by a constant torque, and different rotors interact via a repulsive potential with a surface friction. To focus our study on confinement-induced inhomogeneity, we only allow a radial repulsive interaction between the wall and the particles. The particle dynamics is described by the underdamped Langevin equation. In experiments, a circular vessel containing a monolayer of gear-like granular rotors (Fig. 1*B*) is mounted on an electromagnetic shaker, and the rotors' spinning is driven by vertical vibration. To compare the simulations with the experiments, we use a dimensionless number, ω_s/D_r, to characterize the motility of an isolated rotor for both systems. Here, ω_s and D_r refer to the spin velocity and the rotational diffusion coefficient of the isolated rotor, respectively. The experimental ω_s/D_r is measured as 6.2 (*SI Appendix*), and we choose $\omega_s/D_r = 6.0$ in simulations.

Oscillating Collective Edge Flow. We first consider a fluid system with the packing fraction $\rho = 0.6$ in simulation (Movie S1). Following previous work (12, 32), we measure the steady-state mean tangential velocity of the particles in different concentric annuli, v_t (parallel to the boundary), to quantify the collective motion. Note that the mean radial velocity normal to the wall, v_r, vanishes due to the confinement. Fig. 2*B* displays the orbital angular velocity of the rotor fluid, $v_t(r)/r$, as a function of the distance from the system center, r. Throughout the paper, the orbital angular velocity is normalized by the spin velocity of the isolated rotor, ω_s. Indeed, there exists an edge flow near the boundary. Interestingly, the $v_t(r)/r$ varies nonmonotonously with the distance and exhibits a significant oscillation in space and even changes the sign. The oscillation period of the collective motion is equal to the rotor diameter. The magnitude of the oscillation decays substantially as r decreases and vanishes far away from the boundary, indicating that the edge flow is localized near the boundary. Previous studies on the confined spinners also reveal the emergence of the edge flow, but with no oscillation (12, 32, 33).

To understand the microscopic mechanism of the spatially oscillating edge flow, we note that the existence of the confinement breaks the spatial uniformity of the system. Thus, the environment felt by the particles close to the boundary is considerably different from that far from the boundary. Particularly, the boundary wall can induce a spatially oscillating particle distribution in passive fluids to minimize the system free energy (35, 36). The number density distribution, $n(r)$, of the active rotors is also plotted in Fig. 2*B* and exhibits a behavior similar to that of the passive system (*SI Appendix*), implying that the structural properties of the chiral active system are insensitive to the spin. Based on the spatial inhomogeneity and the active spinning, the driving force for the edge flow can be easily identified. As illustrated in Fig. 2*A*, the particles in the outermost layer, i.e., rotor 1, experience a tangential force from rotor 2, $\mathbf{F}_{21}$, generated due to the friction between the spinning particles. Because the confinement wall is smooth and applies no tangential force on rotor 1, $\mathbf{F}_{21}$ drives rotor 1 to move counterclockwise. Nevertheless, for the particles in other layers, e.g., rotor 2, the outer-layer rotor 1 and the inner-layer rotor 3 contribute opposite frictional forces $\mathbf{F}_{12}$ and $\mathbf{F}_{32}$ on it. If the number density of the inner layer is higher than that of the outer layer, the inner layer will, on average, apply a larger tangential friction, and, hence, rotor 2 will move counterclockwise; otherwise, it will move clockwise. Therefore, the oscillating number density distribution, which has an equilibrium structural origin, can give rise to a position-dependent (spatially oscillatory) frictional stress, which then drives an oscillating edge flow in space. Far away from the boundary, the system density as well as the frictional stress tends to be homogeneous, and, hence, the macroscopic flow vanishes. Such a scenario is formulated via a continuum hydrodynamic theory in *Theoretical Description for the Oscillating Edge Flow*.

The corresponding experimental results are given in Fig. 2*C*, which plots the orbital angular velocity of the granular spinners (Fig. 1*B*) with a low packing fraction $\rho = 0.65$ (the ratio of the area occupied by the particles to that of the vessel). The results also show a spatially oscillating edge flow (Movie S2), with the period being around the spinner diameter. Although the granular spinners are macroscopic and dissipative, confinement can still lead to a spatially inhomogeneous density distribution similar to the simulation. Consequently, the essential requirements for the emergence of oscillating collective motion (i.e., nonuniformity, spin, and interparticle friction) are properly satisfied. The experimental results thus provide strong support for our theoretical predictions.

Nevertheless, two apparent distinctions exist between the simulation and the experiment. One is that $v_t(r)/r$ of the simulation oscillates around zero (Fig. 2*B*), while in the experiment, $v_t(r)/r$ oscillates around a reference value that decays substantially with decreasing r (Fig. 2*C*). The other is that the oscillation magnitude of the simulation $v_t(r)/r$ is stronger than that of the experimental $v_t(r)/r$. We speculate that these discrepancies come from the following facts. In the experiment, the shaken

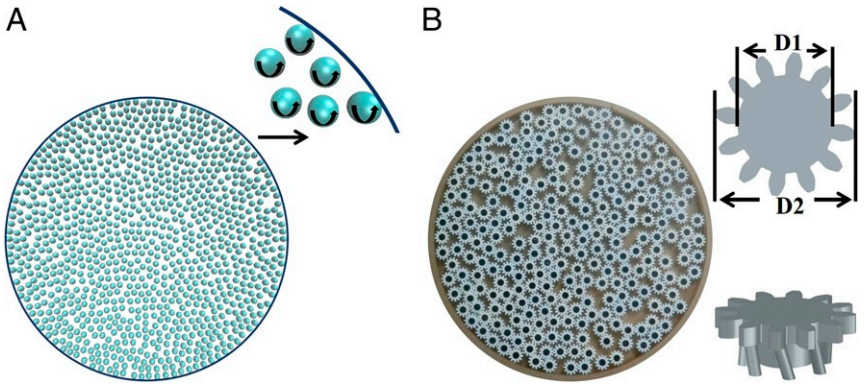

Fig. 1. (*A*) Simulation snapshot of 1,000 spinning disks in confinement, with the packing fraction $\rho = 0.6$, where *Inset* shows a zoomed-in image. (*B*) Experimental snapshot of the gear-like spinners in a circular vessel with $\rho = 0.65$. *Lower Inset* is the sketch (side view) of a 3D-printed active rotor, and *Upper Inset* is the top view of the rotor with D1 = 15.50 ± 0.06 mm and D2 = 21.26 ± 0.06 mm.

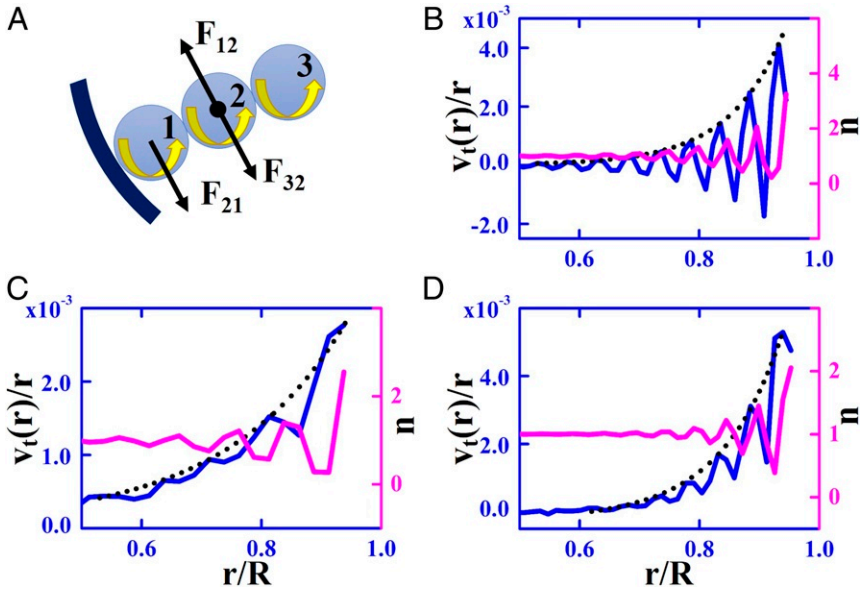

Fig. 2. (*A*) Schematic diagram for the microscopic mechanism of the collective motion in the confined active rotor system. (*B–D*) The orbital angular velocity and the particle number density distribution (normalized by the mean particle number density) as a function of the distance to the system center: simulation results with $\gamma = 100$ (*B*), experimental results (*C*), and simulation results with $\gamma = 2$ (*D*), where the blue lines and the left vertical axis refer to the angular velocity, the magenta lines and the right vertical axis refer to the number density distribution, and the dashed lines are an exponential fit to the peak values of the orbital angular velocity.

gears often separate from the baseplate so that their translational friction with the substrate is greatly weakened. Besides, the gear–gear interactions possess multiple characteristic lengths, e.g., the summit–summit and summit–cleft distances. To account for these aspects in the simulation, we first decrease the translational frictional coefficient, γ, and then use a binary mixture of spinning disks of different sizes (with the size ratio $\simeq 1.3$, roughly mimicking the multiple coupling lengths). The simulation results of the modified model are displayed in Fig. 2*D*, which is in good agreement with the experimental results in Fig. 2*C* and supports our speculation.

Theoretical Description for the Oscillating Edge Flow. To better clarify the underlying mechanism of the spatially oscillating collective motion, we use a two-dimensional (2D) continuum hydrodynamic theory (12) to describe the chiral active fluid. Importantly, we consider a position-dependent frictional stress induced by the inhomogeneous distribution of the rotors, which is essential for the emergence of the oscillatory edge flow in terms of *Oscillating Collective Edge Flow*. The hydrodynamic variables are the mass density of spinners $\varrho(\mathbf{r}, t)$, the momentum density $\varrho(\mathbf{r}, t)\mathbf{v}(\mathbf{r}, t)$, and the angular momentum density $I(\mathbf{r}, t)\omega(\mathbf{r}, t)$, with $I(\mathbf{r}, t)$ the spinner moment of inertia density, which, respectively, obey the conservations of mass, momentum, and angular momentum. The mass-continuity equation reads

$$(\partial_t + \mathbf{v}\cdot\nabla + \nabla\cdot\mathbf{v})\varrho = 0. \qquad [1]$$

In a polar coordinate system, $\nabla = \hat{r}\partial_r + \hat{\phi}\frac{1}{r}\partial_\phi$ and $\mathbf{v} = \hat{r}v_r + \hat{\phi}v_t$ with $\hat{r}$ and $\hat{\phi}$ separately being the radial and tangential unit vectors. In the steady state, $v_r(\mathbf{r}) = 0$ together with the system symmetry imply $\mathbf{v}\cdot\nabla\varrho = 0$, such that Eq. **1** becomes

$$\nabla\cdot\mathbf{v} = 0, \qquad [2]$$

although the chiral active fluid under study is compressible.

The conservation of momentum takes the form,

$$\varrho(\partial_t + \mathbf{v}\cdot\nabla)v_i = \partial_j\sigma_{ij} - \Gamma v_i, \qquad [3]$$

with Γ the frictional coefficient from environment, which is related to the frictional coefficient of single spinner by $\Gamma = \gamma n = 4\gamma\rho/\pi\sigma_s^2$. And the stress tensor, σ_{ij}, is expressed as

$$\sigma_{ij} = -p\delta_{ij} + \eta(\partial_i v_j + \partial_j v_i) + \epsilon_{ij}\eta_R(2\omega - \Omega), \qquad [4]$$

where η is the shear viscosity, ϵ_{ij} the Levi–Civita symbol, $\Omega = \hat{\mathbf{z}}\cdot(\nabla\times\mathbf{v}) = \epsilon_{ij}\partial_i v_j$ the vorticity of the flow field, and η_R the rotational viscosity that arises from interrotor friction. In Eq. **4**, the last term refers to the antisymmetric frictional stress that couples the spin to the flow; the bulk viscosity term is absent owing to Eq. **2**, and the odd viscosity term (30, 31) is ignored, as it can be absorbed in the pressure p and does not contribute to the tangential stress. The shear and rotational viscosities are position-dependent via the confinement-induced inhomogeneity of packing fraction. We here focus on the inhomogeneous η_R that is the origin of the oscillatory edge flow. Since η_R results from the interparticle frictional collisions, it is proportional to the spinner packing fraction and the collision frequency of a tagged spinner with its surrounding particles. From the Enskog theory, the collision frequency can be approximately estimated as $8\rho g(\sigma_s)\sqrt{k_B T/\pi m\sigma_s^2}$ (37), with $g(\sigma_s)$ the pair correlation function at contact. Thus, we have $\eta_R = A\rho^2 g(\sigma_s)$ with A an unknown prefactor. A virial expansion yields $g(\sigma_s) = \frac{1-7\rho/16}{(1-\rho)^2} - \frac{\rho^3/16}{8(1-\rho)^4}$ (38), such that the rotational viscosity becomes

$$\eta_R(\rho) = A\rho^2\left[\frac{1-7\rho/16}{(1-\rho)^2} - \frac{\rho^3/16}{8(1-\rho)^4}\right], \qquad [5]$$

which well fits independent simulation results with the prefactor $A \simeq 2.07$ (*SI Appendix*). Eq. **5** means that the oscillatory profile of the local particle-packing fraction results in a spatially oscillatory η_R (Fig. 3, *Inset*) and, hence, frictional stress.

As the edge flow is weak and the Reynolds number of the chiral active fluid is low (the centripetal acceleration $\varrho\mathbf{v}\cdot\nabla\mathbf{v}$

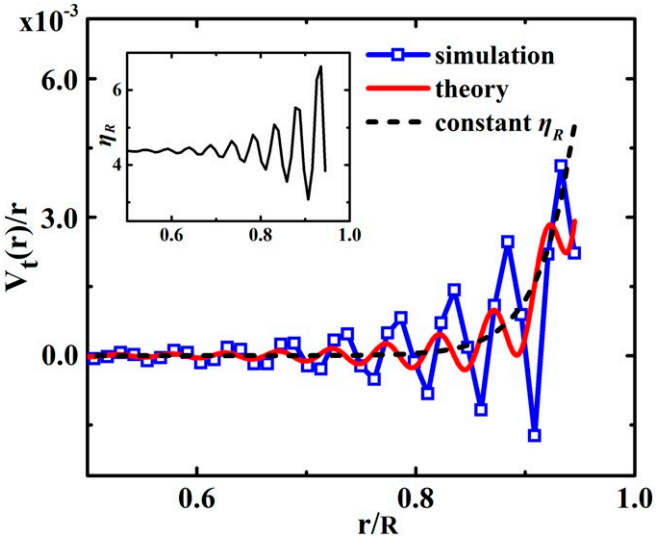

Fig. 3. Comparison of the orbital angular velocities obtained from the simulation (blue square) and the continuum theory with the nonuniform η_R (red solid line). The system is the same as that of Fig. 2*B*. In the theoretical calculation, the position-dependent η_R (*Inset*) is introduced by substituting the packing fraction profile from the simulation measurement into Eq. **5**. For comparison, we also plot the theoretically calculated v_t/r for an incompressible fluid of rotors (i.e., constant η_R; black dashed line), and the calculation details are provided in *SI Appendix*.

is negligible), from Eqs. **3** and **4**, the steady-state equation of momentum conservation thus is

$$0 = -\partial_i p + \eta\nabla^2 v_i + \epsilon_{ij}\partial_j[\eta_R(2\omega - \Omega)] - \Gamma v_i. \quad [6]$$

Here, for simplicity, η is regarded as a constant and equals to its value in the bulk, $\eta \simeq 25$, which can be determined from independent simulations by externally imposing a shear flow in an unconfined active fluid (*SI Appendix*).

The angular momentum conservation is written as

$$I(\partial_t + \mathbf{v}\cdot\nabla)\omega = -\Gamma_r\omega - 2\eta_R(2\omega - \Omega) + D_\omega\nabla^2\omega + \tau, \quad [7]$$

where Γ_r refers to the rotational friction coefficient from environment, D_ω to the diffusion coefficient, and τ to the torque density field. Γ_r and τ are, respectively, related to their single-particle counterparts, γ_r and $\mathbf{T}_d$, by $\Gamma_r = 4\gamma_r\rho/\pi\sigma_s^2$ and $\tau = 4\mathbf{T}_d\rho/\pi\sigma_s^2$. In the steady state, $\mathbf{v}\cdot\nabla\omega = 0$, and thus Eq. **7** reduces to

$$0 = -\Gamma_r\omega - 2\eta_R(2\omega - \Omega) + D_\omega\nabla^2\omega + \tau. \quad [8]$$

In the present packing fraction ($\rho = 0.6$), the diffusion coefficient D_ω is small such that the diffusion term in Eq. **8** can be safely neglected. The spin angular velocity thus approximately reads

$$\omega = \frac{\tau + 2\eta_R\Omega}{\Gamma_r + 4\eta_R}. \quad [9]$$

Inserting Eq. **9** into Eq. **6**, we have for the tangential component of the momentum equation in polar coordinates,

$$\beta\partial_r^2 v_t + \frac{\partial_r(\beta r)}{r}\partial_r v_t - \frac{(\beta - r\partial_r\beta + r^2\Gamma)}{r^2}v_t - 2\partial_r\beta' = 0, \quad [10]$$

where $\beta = \eta + \Gamma_r\eta_R(\Gamma_r + 4\eta_R)^{-1}$ and $\beta' = \beta\tau(\Gamma_r + 4\eta_R)^{-1}$ are defined. Thus, the edge flow can be obtained by solving Eq. **10**, with the boundary condition $v_t(r = 0) = 0$, which arises from the rapid decay of the edge flow, and the frictionless boundary condition at the confined sidewall, $\sigma_{\phi r}(R - \sigma_s) = \left[\eta_R\left(\partial_r v_t + \frac{v_t}{r} - 2\omega\right) + \eta\left(\partial_r v_t - \frac{v_t}{r}\right)\right]_{r=R-\sigma_s} = 0$. Fig. 3 plots the theoretical orbital angular velocity that reproduces all of the features of the oscillatory edge flow obtained from the simulation. Nevertheless, the theoretical calculation underestimates the oscillation magnitude by a factor of around two, which may be attributed to the approximations employed in the theoretical derivation. In addition, there is apparently a phase shift between the theoretical calculation and the simulation, which originates from the following fact. The continuum theory neglects the finite size of the rotor, so that the fluid flow is driven by the local gradient of the frictional stress, while in the simulations, the fluid flow is produced by the variation of the frictional stress on the length scale of the rotor size. Except for the quantitative differences, the theoretical calculation compares well to the simulation measurement, confirming the microscopic mechanism of the oscillatory edge flow proposed in *Oscillating Collective Edge Flow*. With the obtained v_t, the spin angular velocity is determined via Eq. **9**, which also agrees well with that measured in the simulation (*SI Appendix*). Further verification of the continuum theory is given in *SI Appendix* by exploring wider parameter spaces.

Collective Motion Modes of Higher Densities. The nonuniform particle distribution has been shown to be critical for the emergence of the oscillating edge flow, which highlights the importance of the compressibility of the chiral active system. To further study the effect of the compressibility on the collective motion, we consider the simulation systems with a wide range of packing fraction from $\rho = 0.50$ to 0.82. Interestingly, we find three different modes of collective motion as ρ increases, as shown in Fig. 4*A*. For low $\rho = 0.6$, the collective flow oscillates around zero, and the magnitude decays to zero as r decreases. The decaying $v_t(r)/r$ is reminiscent of the circular Couette flow of a viscous fluid confined in two concentric cylinders (39), in which the outer cylinder rotates at constant angular velocity, while the inner cylinder remains fixed. This implies that the chiral active system of low ρ is in the fluid regime. For high $\rho = 0.8$, the system rotates as a rigid body at a constant angular velocity without any periodic oscillation (only with fluctuation). In this case, the system is an elastic solid. At moderate $\rho = 0.7$, the $v_t(r)/r$ oscillates around a constant nonzero value (without decay), indicating that different domains of the active system can slide over each other and, at the same time, are constrained in an elastic background.

For comparison, we also plot the orbital angular velocity of the experimental spinners at low ($\rho = 0.65$) and moderate ($\rho = 0.78$) packing fractions, as shown in Fig. 4*B*. The experimental results are consistent with the simulation in Fig. 4*A*. Here, an experimental system of high ρ like a rigid body cannot be achieved due to the gear-like structure of the particles, so the corresponding results are not provided.

Structural Origins of the Transitions between Different Modes. To elucidate the structural origin of different modes of the collective motion, we measure the orientational order parameter $\psi_{6j} = (\sum_{k\in N_j} e^{6i\theta_{jk}})/N_j$ in the simulations (Fig. 5*A*), which characterizes local crystalline order (40, 41). Here, the sum is taken over the N_j nearest neighbors of particle j, and θ_{jk} is the angle between $\mathbf{r}_k - \mathbf{r}_j$ and a fixed arbitrary axis. At $\rho = 0.60$, the mean ψ_{6j} is small, and the system is in a viscous fluid regime. In this case, the particles can easily change their positions and cannot sustain a rigid rotation (Movie S1). At $\rho = 0.80$, most areas (except for the boundary region) have quite large ψ_{6j}, and the inner-layer particles form a defect-free crystal. Thus, the active particles cannot change their relative positions, only allowing a whole rotation (Movie S3). Nevertheless, for

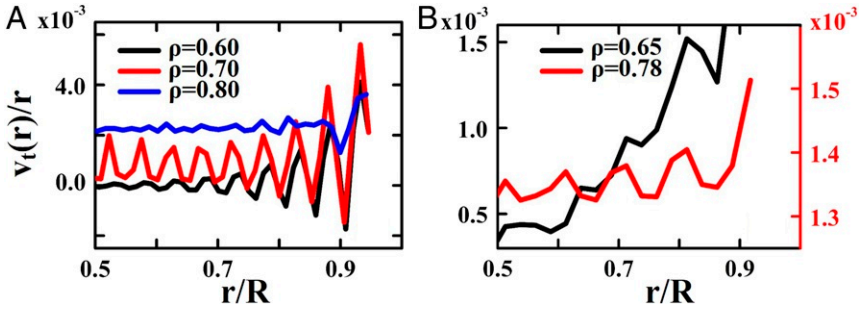

Fig. 4. (*A*) The orbital angular velocity of different collective motion modes for $\rho = 0.60, 0.70, 0.80$ in simulation. (*B*) Experimental results for low and moderate packing fractions, where the $v_t(r)/r$ at the moderate packing fraction is displayed on the right red vertical axis.

$\rho = 0.70$, the regions of high ψ_{6j} percolate and form a solid-like framework; meanwhile, some defects with low ψ_{6j} distribute randomly (Movie S4). Owing to the presence of the defects, the active rotors can rearrange their positions in the elastic background, exhibiting a "viscoelastic" collective motion. Similar structural analyses on the experimental systems are carried out in *SI Appendix*.

We now investigate the transitions between the various modes of collective motion. To do this, we analyze the $v_t(r)/r$ curves for a wide range of ρ. The reference value $[v_t(r)/r]_0$, i.e., the average of $v_t(r)/r$ in the bulk, is used to distinguish the viscoelastic mode ($[v_t(r)/r]_0 > 0$) from the collective motion of the viscous fluid ($[v_t(r)/r]_0 = 0$). Fig. 5*B* clearly shows that $[v_t(r)/r]_0$ starts to have a positive value at $\rho \simeq 0.64$, marking the first transition point. The oscillation quality distinguishes the viscoelastic mode (oscillation) from the collective rotation of the elastic solid (fluctuation). The oscillation quality can be quantified by the autocorrelation function of $s_i(r) \equiv v_t(r)/r - \langle v_t(r)/r \rangle$ for each curve, $C(d) = \langle s_i(r)s_i(r+d) \rangle / \nu^2$ (42), with ν the SD of $s_i(r)$, d the distance lag, and $\langle \cdot \rangle$ a spatial average. $C(d)$ oscillates for perfect oscillations, but quickly vanishes for pure fluctuations. The first positive peak C_1 of $C(d)$ characterizes the quality of an oscillation, which decreases as ρ increases (Fig. 5*C*). C_1 shows a very steep descent around $\rho \simeq 0.8$, which thus establishes a reasonable border between oscillation and fluctuation and, hence, corresponds to the second transition point.

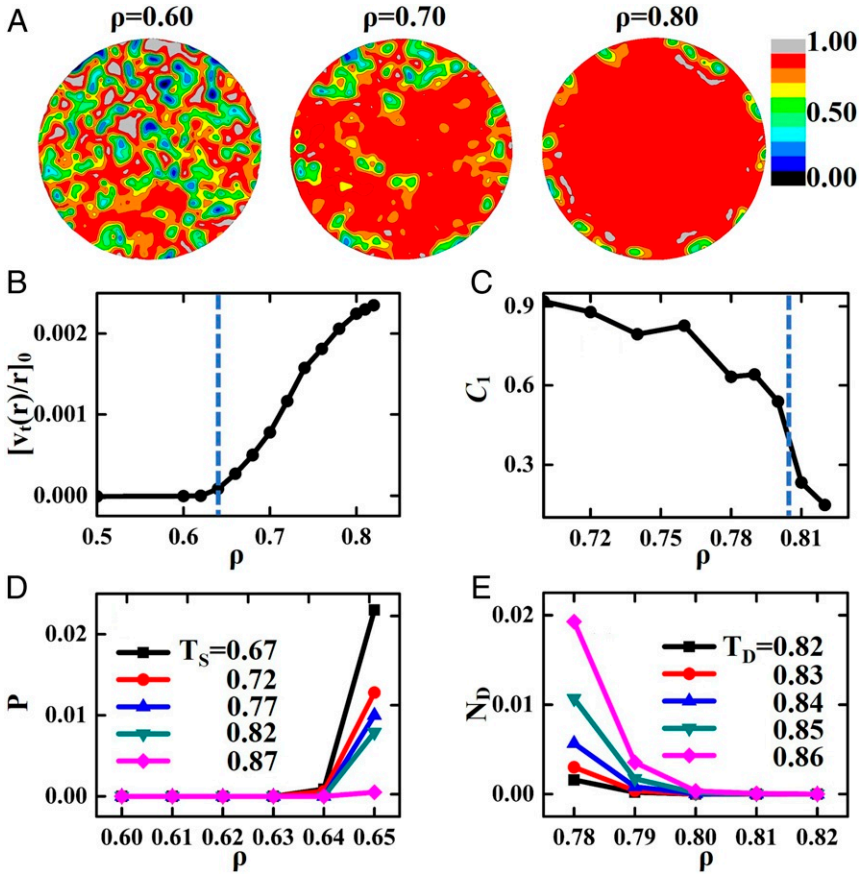

Fig. 5. (*A*) Contours of the orientational order parameter ψ_{6j} for low ($\rho = 0.60$), moderate ($\rho = 0.70$), and high ($\rho = 0.80$) densities. (*B*) The reference angular velocity as a function of ρ, where the dashed line marks the transition point. (*C*) The first positive peak value of the autocorrelation function $C(d)$ as a function of ρ, with the steepest descent point marked by the dashed line. (*D*) The probabilities of percolation for different thresholds ($2\tau_S R$). (*E*) The mean numbers of defects, determined by $\psi_{6j} < \tau_D$, with various τ_D being taken.

Transitions between various modes must arise from the structural changes of the chiral active matter. According to the previous discussions, the structural changes correspond to the percolation of the solid-like regions or the formation of a defect-free crystal. Fig. 5*D* plots the probability of the percolation as a function of ρ. Here, the percolation is thought to occur once the x or y dimension of the connected solid-like region [i.e., region with $\psi_{6j} \geq 0.84$ (43)] is greater than a threshold size $2\mathrm{T}_S R$, with T_S an imposed number; and the percolation probability is estimated as the average percolation frequency per frame. Clearly, the percolation probability becomes nonzero at $\rho = 0.64$, which agrees quantitatively with the first transition point of the motion mode given in Fig. 5*B*. (Note that the percolation here does not necessarily indicate a liquid-to-hexatic phase transition, given that our system is too small to distinguish whether there exists a long-range correlation.) Fig. 5*E* plots the mean number of defects, N_D, per frame in the bulk as a function of ρ. Here, a defect is defined as a region with ψ_{6j} less than a prescribed value T_D. The results show that the defects occur only when $\rho \leq 0.8$, which is perfectly consistent with the second transition point of the motion mode, as determined in Fig. 5*C*. Thus, we clarify the microscopic structural origins of the transitions between the different modes of collective motion.

Discussion

The emergent collective motion of the confined active rotors has been studied numerically, theoretically, and experimentally. Remarkably, this minimal chiral active matter exhibits rich collective behavior, resulting from an inhomogeneous density distribution induced by confinement boundary. In particular, the collective motion has a significant spatial oscillation and experiences three different modes as the packing fraction changes. The microscopic mechanisms underlying the collective behaviors have been elucidated: The position-dependent frictional stress drives an oscillating edge flow; the percolation of solid-like regions induces the penetration of the oscillation into the bulk; and the vanishing of defects disables the rearrangement of particle positions, resulting in a rigid rotation of the bulk. Our findings highlight the importance of the compressibility and the confinement-induced inhomogeneity in the oscillatory collective motion of chiral active system and also the influence of nonequilibrium structure on dynamics of active matter.

Methods

Simulation. Different rotors interact via a repulsive Lennard–Jones (LJ) type of potential, $U(r) = 4\epsilon\left[\left(\frac{\sigma_s}{r}\right)^{2l} - \left(\frac{\sigma_s}{r}\right)^{l}\right] + \epsilon$, with r being the distance between rotor centers. Here, we set the disk diameter $\sigma_s = 2$, the interaction intensity $\epsilon = 1$, and the potential stiffness $l = 12$. Besides the radial potential interaction, different disks also couple tangentially through a surface friction realized by the bounce-back collision (44). The interaction between the boundary wall and the rotors is chosen as the repulsive LJ potential with $l = 24$ and the interaction length σ_s, without any friction. In simulations, N = 1,000 is fixed, and the packing fraction is adjusted by changing R.

The translational degree of freedom of the active particles satisfies the underdamped Langevin equation (44),

$$m\dot{\mathbf{v}} = \mathbf{F}_r + \mathbf{F}_w + \boldsymbol{\eta} - \gamma\mathbf{v}, \qquad [11]$$

with $m = 1$ being the particle mass, $\gamma = 100$ the translational friction coefficient, and $\mathbf{F}_r$ and $\mathbf{F}_w$ the interparticle and particle-wall steric forces, respectively. Here, the stochastic force $\boldsymbol{\eta}$ is Gaussian distributed with $\langle\boldsymbol{\eta}(t)\rangle = 0$ and $\langle\boldsymbol{\eta}(t)\boldsymbol{\eta}(t')\rangle = 2k_{\mathrm{B}}T\gamma\delta(t-t')$, with the temperature $k_{\mathrm{B}}T = \epsilon$. Similarly, the spin-angular velocity of the particles evolves according to

$$I_s\dot{\boldsymbol{\omega}} = \mathbf{T}_d + \boldsymbol{\xi} - \gamma_r\boldsymbol{\omega}, \qquad [12]$$

where $I_s = \frac{1}{8}m\sigma_s^2$ refers to the rotor momenta of inertia, $\gamma_r = \frac{1}{3}\sigma_s^2\gamma$ the rotational friction coefficient, $\mathbf{T}_d = 6$ the driving torque, and $\boldsymbol{\xi}$ the Gaussian distributed stochastic torque with zero mean and $\langle\boldsymbol{\xi}(t)\boldsymbol{\xi}(t')\rangle = 2k_{\mathrm{B}}T\gamma_r\delta(t-t')$. In addition, the bounce-back collision (44) that generates the friction between two rotors in contact (say, i and j) can be realized by instantaneously updating $\mathbf{v}$ and $\boldsymbol{\omega}$, according to $\delta\mathbf{v}_i = \delta\mathbf{p}_i/m$ and $\delta\boldsymbol{\omega}_i = -\frac{1}{2}\mathbf{r}_{ij} \times \delta\mathbf{p}_i/I$. Here, the impulse $\delta\mathbf{p}_i$ is determined by conservation laws,

$$\delta\mathbf{p}_i = -m\left(\tilde{\mathbf{v}}_{ij}^{\parallel} + \frac{\kappa}{1+\kappa}\tilde{\mathbf{v}}_{ij}^{\perp}\right), \qquad [13]$$

with the parameter $\kappa = 4I_s/m\sigma_s^2$, and $\tilde{\mathbf{v}}_{ij}^{\parallel}$ and $\tilde{\mathbf{v}}_{ij}^{\perp}$ the components of the relative velocity at collision point, $(\mathbf{v}_i - \mathbf{v}_j) - \frac{1}{2}(\boldsymbol{\omega}_i + \boldsymbol{\omega}_j) \times (\mathbf{r}_i - \mathbf{r}_j)$, parallel and perpendicular to $\mathbf{r}_i - \mathbf{r}_j$, respectively. The velocity Verlet algorithm is used to integrate the equations of motion with the time step $\Delta t = 10^{-3} \times \sqrt{m\sigma_s^2/\epsilon}$.

The rotors are initially randomly distributed; 10^5 steps are performed to eliminate the effects of the initial configuration, and 6.4×10^9 steps are performed to compute the physical quantities. To measure the orbital angular velocity v_t/r and the number density distribution n of the rotors, we divide the system into concentric annuli, with the width $\Delta r = \frac{1}{4}\sigma_s$.

Experiment. Gear-like rotors are put in a circular vessel mounted on an electromagnetic shaker. An acrylic cover placed on the top of the vessel can suppress vertical motion of the particles, and thus ensure that the particles move horizontally on the 2D baseplate. The shaker provides a vertical vibration $Z = A\sin(2\pi ft)$, with f the vibration frequency and A the vibration amplitude. The vibration strength is characterized by $\Gamma = A(2\pi f)^2/g$, with g the gravitational acceleration. Experiments are performed with $f = 50$ *Hz* and $\Gamma = 1.7$. A high-resolution camera system is used to track the particle trajectories.

The granular rotors used in our experiment are similar to those in previous work (45–48). The particles rest on circularly aligned tilted legs (Fig. 1*B*), which are manufactured from polylactide by using a three-dimensional (3D) printer. Owing to geometric asymmetry, the tilted legs act as elastic springs and transfer vibrational energy from the shaker into a unidirectional rotation of the rotor without active translation. The distribution of translational displacement of a single rotor is symmetrical with respect to the origin, suggesting that the rotor indeed performs an unbiased random walk (*SI Appendix*). The interactions between rotors are short-ranged repulsive. The protruding teeth of the gear-like rotors can significantly enhance the interparticle friction. Nevertheless, disc-shaped rotors made of a material with a large friction coefficient are expected to exhibit similar collective behavior. The effect of interrotor friction on the collective motion is studied by simulation and theory (*SI Appendix*).

Data Availability. All data discussed in the paper are available in the main text and *SI Appendix*.

ACKNOWLEDGMENTS. We thank T. C. Lubensky, D. Frenkel, R. Podgornik, and R. Blumenfeld for helpful discussions. This work was supported by National Natural Science Foundation of China Grants 11874397, 11674365, and 11774394; Key Research Program of Frontier Sciences of Chinese Academy of Sciences Grant QYZDB-SSW-SYS003; and the K. C. Wong Education Foundation.

1. S. Ramaswamy, The mechanics and statistics of active matter. *Annu. Rev. Condens. Matter Phys.* **1**, 323–345 (2010).
2. T. Vicsek, A. Zafeiris, Collective motion. *Phys. Rep.* **517**, 71–140 (2012).
3. M. E. Cates, Diffusive transport without detailed balance in motile bacteria: Does microbiology need statistical physics? *Rep. Prog. Phys.* **75**, 042601 (2012).
4. M. C. Marchetti *et al.*, Hydrodynamics of soft active matter. *Rev. Mod. Phys.* **85**, 1143–1189 (2013).
5. J. Elgeti, R. G. Winkler, G. Gompper, Physics of microswimmers—single particle motion and collective behavior: A review. *Rep. Prog. Phys.* **78**, 056601 (2015).
6. C. Bechinger *et al.*, Active particles in complex and crowded environments. *Rev. Mod. Phys.* **88**, 045006 (2016).
7. H. P. Zhang, A. Be'er, E. L. Florin, H. L. Swinney, Collective motion and density fluctuations in bacterial colonies. *Proc. Natl. Acad. Sci. U.S.A.* **107**, 13626–13630 (2010).
8. I. Theurkauff, C. Cottin-Bizonne, J. Palacci, C. Ybert, L. Bocquet, Dynamic clustering in active colloidal suspensions with chemical signaling. *Phys. Rev. Lett.* **108**, 268303 (2012).
9. I. Buttinoni *et al.*, Dynamical clustering and phase separation in suspensions of self-propelled colloidal particles. *Phys. Rev. Lett.* **110**, 238301 (2013).
10. H. Noji, R. Yasuda, M. Yoshida, K. Kinosita Jr, Direct observation of the rotation of F1-ATPase. *Nature* **386**, 299–302 (1997).

11. J. M. Catchmark, S. Subramanian, A. Sen, Directed rotational motion of microscale objects using interfacial tension gradients continually generated via catalytic reactions. *Small* **1**, 202–206 (2005).
12. J. C. Tsai, F. Ye, J. Rodriguez, J. P. Gollub, T. C. Lubensky, A chiral granular gas. *Phys. Rev. Lett.* **94**, 214301 (2005).
13. M. Yang, M. Ripoll, A self-propelled thermophoretic microgear. *Soft Matter* **10**, 1006–1011 (2014).
14. M. Yang, M. Ripoll, K. Chen, Catalytic microrotor driven by geometrical asymmetry. *J. Chem. Phys.* **142**, 054902 (2015).
15. C. Maggi, F. Saglimbeni, M. Dipalo, F. De Angelis, R. D. Leonardo, Micromotors with asymmetric shape that efficiently convert light into work by thermocapillary effects. *Nat. Commun.* **6**, 7855 (2015).
16. T. Vicsek, A. Czirók, E. Ben-Jacob, I. Cohen, O. Shochet, Novel type of phase transition in a system of self-driven particles. *Phys. Rev. Lett.* **75**, 1226–1229 (1995).
17. J. Toner, Y. Tu, Long-range order in a two-dimensional dynamical *XY* model: How birds fly together. *Phys. Rev. Lett.* **75**, 4326–4329 (1995).
18. G. Grégoire, H. Chaté, Onset of collective and cohesive motion. *Phys. Rev. Lett.* **92**, 025702 (2004).
19. F. D. C. Farrell, M. C. Marchetti, D. Marenduzzo, J. Tailleur, Pattern formation in self-propelled particles with density-dependent motility. *Phys. Rev. Lett.* **108**, 248101 (2012).
20. A. Bricard, J.-B. Caussin, N. Desreumaux, O. Dauchot, D. Bartolo, Emergence of macroscopic directed motion in populations of motile colloids. *Nature* **503**, 95–98 (2013).
21. J. A. Cohen, R. Golestanian, Emergent cometlike swarming of optically driven thermally active colloids. *Phys. Rev. Lett.* **112**, 068302 (2014).
22. M. E. Cates, J. Tailleur, Motility-induced phase separation. *Annu. Rev. Condens. Matter Phys.* **6**, 219–244 (2015).
23. I. H. Riedel, K. Kruse, J. Howard, A self-organized vortex array of hydrodynamically entrained sperm cells. *Science* **309**, 300–303 (2005).
24. A. P. Petroff, X. L. Wu, A. Libchaber, Fast-moving bacteria self-organize into active two-dimensional crystals of rotating cells. *Phys. Rev. Lett.* **114**, 158102 (2015).
25. X. Chen, X. Yang, M. Yang, H. P. Zhang, Dynamic clustering in suspension of motile bacteria. *Europhys. Lett.* **111**, 54002 (2015).
26. J. Palacci, S. Sacanna, A. P. Steinberg, D. J. Pine, P. M. Chaikin, Living crystals of light-activated colloidal surfers. *Science* **339**, 936–940 (2013).
27. H. Wioland, F. G. Woodhouse, J. Dunkel, J. O. Kessler, R. E. Goldstein, Confinement stabilizes a bacterial suspension into a spiral vortex. *Phys. Rev. Lett.* **110**, 268102 (2013).
28. E. Lushi, H. Wioland, R. E. Goldstein, Fluid flows created by swimming bacteria drive self-organization in confined suspensions. *Proc. Natl. Acad. Sci. U.S.A.* **111**, 9733–9738 (2014).
29. A. Bricard *et al.*, Emergent vortices in populations of colloidal rollers. *Nat. Commun.* **6**, 7470 (2015).
30. D. Banerjee, A. Souslov, A. G. Abanov, V. Vitelli, Odd viscosity in chiral active fluids. *Nat. Commun.* **8**, 1573 (2017).
31. V. Soni *et al.*, The odd free surface flows of a colloidal chiral fluid. *Nat. Phys.* **15**, 1188–1194 (2019).
32. B. C. Van Zuiden, J. Paulose, W. T. M. Irvine, D. Bartolo, V. Vitelli, Spatiotemporal order and emergent edge currents in active spinner materials. *Proc. Natl. Acad. Sci. U.S.A.* **113**, 12919–12924 (2016).
33. X. Yang, C. Y. Ren, K. J. Cheng, H. P. Zhang, Robust boundary flow in chiral active fluid. *Phys. Rev. E* **101**, 022603 (2020).
34. K. Dasbiswas, K. K. Mandadapu, S. Vaikuntanathan, Topological localization in out-of-equilibrium dissipative systems. *Proc. Natl. Acad. Sci. U.S.A.* **115**, E9031–E9040 (2018).
35. I. K. Snook, W. Van Megen, Solvation forces in simple dense fluids. I. *J. Chem. Phys.* **72**, 2907–2913 (1980).
36. H. Reich, M. Schmidt, Capillary nematization of hard colloidal platelets confined between two parallel hard walls. *J. Phys. Condens. Matter* **19**, 326103 (2007).
37. L. H. Ning *et al.*, Universal scaling law for colloidal diffusion in complex media. *Phys. Rev. Lett.* **122**, 178002 (2019).
38. S. Luding, Global equation of state of two-dimensional hard sphere systems. *Phys. Rev. E* **63**, 042201 (2001).
39. A. Davey, The growth of Taylor vortices in flow between rotating cylinders. *J. Fluid. Mech.* **14**, 336–368 (1962).
40. Y. Han, NY. Ha, A. M. Alsayed, A. G. Yodh, Melting of two-dimensional tunable-diameter colloidal crystals. *Phys. Rev. E* **77**, 041406 (2008).
41. F. Wang, D. Zhou, Y. Han, Melting of colloidal crystals. *Adv. Funct. Mater.* **26**, 8903–8919 (2016).
42. R. Liu, M. Yang, K. Chen, M. Hou, K. To, Coupled leidenfrost states as a monodisperse granular clock. *Phys. Rev. E* **94**, 020901 (2016).
43. K. Watanabe, H. Tanaka, Direct observation of medium-range crystalline order in granular liquids near the glass transition. *Phys. Rev. Lett.* **100**, 158002 (2008).
44. M. P. Allen, D. J. Tildesley, *Computer Simulation of Liquids* (Oxford University Press, Oxford, UK, 2017).
45. C. Scholz, S. D'Silva, T. Pöschel, Ratcheting and tumbling motion of vibrots. *New J. Phys.* **18**, 123001 (2016).
46. C. Scholz, T. Pöschel, Velocity distribution of a homogeneously driven two-dimensional granular gas. *Phys. Rev. Lett.* **118**, 198003 (2017).
47. C. Scholz, M. Engel, T. Pöschel, Rotating robots move collectively and self-organize. *Nat. Commun.* **9**, 931 (2018).
48. E. Altshuler *et al.*, Vibrot, a simple device for the conversion of vibration into rotation mediated by friction: Preliminary evaluation. *PLoS One* **8**, e67838 (2013).